Geophysical Research Letters

RESEARCH LETTER
10.1029/2020GL090313

Key Points:

- The 50°N to 50°S cloud fraction reduced from 0.65 to 0.47 based on new MISR cloud product that corrects for measurement resolution effects
- Largest reductions (up to ~0.4) in cloud fraction occur over trade cumulus regions and smallest (<0.1) occur over stratocumulus regions
- New MISR cloud fractions are within ±0.05–0.08 of regional ASTER benchmarks compared to overestimates of 0.4–0.5 from original MISR and MODIS

Supporting Information:

- Supporting Information S1

Correspondence to:
L. Di Girolamo and S. Dey,
gdi@illinois.edu;
sagnik@cas.iitd.ac.in

Citation:
Dutta, S., Di Girolamo, L., Dey, S., Zhan, Y., Moroney, C. M., & Zhao, G. (2020). The reduction in near-global cloud cover after correcting for biases caused by finite resolution measurements. *Geophysical Research Letters*, *47*, e2020GL090313. https://doi.org/10.1029/2020GL090313

Received 15 AUG 2020
Accepted 8 NOV 2020
Accepted article online 20 NOV 2020

The Reduction in Near-Global Cloud Cover After Correcting for Biases Caused by Finite Resolution Measurements

Soumi Dutta[1], Larry Di Girolamo[2], Sagnik Dey[1], Yizhe Zhan[2], Catherine M. Moroney[3], and Guangyu Zhao[2]

[1]Centre for Atmospheric Sciences, Indian Institute of Technology Delhi, New Delhi, India, [2]Department of Atmospheric Sciences, University of Illinois at Urbana-Champaign, Urbana, IL, USA, [3]Jet Propulsion Laboratory, NASA, Pasadena, CA, USA

Abstract A solution to the common problem that sensors have in overestimating cloud fraction (CF) due to their finite resolution is implemented by the Multi-angle Imaging SpectroRadiometer (MISR) to produce a resolution-corrected CF product. Here we evaluate the efficacy of this product toward the development of an improved global cloud climatology. We found a large reduction in CF across various regions of the globe due to the correction, with reductions >0.4 in regions dominated by shallow cumulus clouds. The MISR resolution-corrected CF lies within ±0.05–0.08 of 180 randomly selected scenes of 15-m resolution Advanced Spaceborne Thermal Emission and Reflection Radiometer (ASTER) data, where MISR uncorrected CF and Moderate Resolution Imaging Spectroradiometer (MODIS) CF overestimated this benchmark by 0.40–0.50. We conclude that the CF between 50°N and 50°S is much lower than that reported by the original MISR and MODIS and that the new MISR cloud product indeed provides improved estimates of CF.

1. Introduction

Clouds are a very important component of the climate system because of their contributions to the Earth's radiation budget and hydrological cycle. They continue to contribute to the largest uncertainty in climate forcing estimates due to poor understanding and representation of cloud feedback processes in climate models (IPCC, 2013; Vial et al., 2013). A step toward resolving this issue is to develop an unbiased, long-term, observation-based climatology of cloud fraction (CF) that is used, in part, to evaluate climate models. The Global Water and Energy Cycle Experiment (GEWEX) Cloud Assessment (Stubenrauch et al., 2012, 2013) was an effort toward achieving this goal. It revealed large discrepancies among 12 publicly available satellite cloud data sets in both global and regional mean cloud cover. For example, the global mean cloud fraction ranged from 0.56 to 0.73, with regional difference topping 0.4 even for the more popular data sets. The reasons for these discrepancies can be broadly categorized as (a) "resolution" effect (e.g., Di Girolamo & Davies, 1997), (b) "view angle" effect (e.g., Minnis, 1989), (c) "diurnal cycle" effect (e.g., Eastman & Warren, 2014), and (d) "instrument sensitivity and methodology" effect (e.g., Stubenrauch et al., 2012).

In this work, we addressed the resolution effect and, in part, the view angle effect. Passive sensors like Multi-angle Imaging SpectroRadiometer (MISR) and Moderate Resolution Imaging Spectroradiometer (MODIS) calculate CF as the ratio of the number of cloudy pixels to the total number of cloudy and clear pixels in a scene (Di Girolamo & Davies, 1997). Choosing a pixel as "cloudy" or "clear" (often referred to as cloud mask) depends on the cloud detection algorithm of the respective instrument (Goodman & Henderson-Sellers, 1988; Rossow et al., 1985). A perfect, clear-conservative cloud mask detects a pixel as "cloudy" if it contains any amount of cloud however defined (Di Girolamo & Davies, 1997). Thus, subpixel clouds lead to overestimated CF, especially in the tropical regions dominated by trade wind cumulus. This overestimation is termed as the "resolution effect," which depends on the instrument resolution with respect to the spatial distribution and size of the clouds (e.g., Dey et al., 2008). MISR opted for a clear-conservative cloud mask for its Radiometric Camera-by-camera Cloud Mask (RCCM) product because (1) aerosol retrievals are a core component of the MISR mission (Diner et al., 1998) and (2) CF biases from resolution effects are well behaved (Di Girolamo & Davies, 1997). This resulted in negligible cumulus cloud contamination

10.1029/2020GL090313

effects on MISR aerosol retrievals (Zhao et al., 2009) and overestimates in CF that resemble behaviors of a clear-conservative cloud mask (Zhao & Di Girolamo, 2006). MODIS also overestimates CF due to the resolution effect but with a behavior that is difficult to characterize (Zhao & Di Girolamo, 2006).

Di Girolamo and Davies (1997) developed several techniques to correct the CF bias due to the resolution effect. One of those is a machine learning pattern recognition technique (a technique which determines the amount of necessary correction based on scene specific information) that was found to result in unbiased estimates of true CF relative to a training data set, but practical application needed to await a globally represented, high-resolution training data. Jones et al. (2012) developed this training set over the ocean from the high-resolution (15 m) Advanced Spaceborne Thermal Emission and Reflection Radiometer (ASTER) on Terra and applied the pattern recognition technique to correct CF estimates from MISR's RCCM. They showed that this technique resulted in a reduction of average MISR CF from 0.50 to 0.20 over the tropical Western Atlantic (10–20°N and 50–60°W). Since 2014, this technique has been included in the standard production of the MISR TC_Classifiers product but has yet to be assessed. This propels the need to carry out a more extensive global analysis to examine the new resolution-corrected MISR RCCM CF product, hereafter referred to as PRCCF (pattern recognition-corrected cloud fraction) and answer the question “Does this product provide improved estimates of global cloud coverage?”

Here we analyze and present a near-global (50°N to 50°S) cloud climatology of an 18-year (March 2000 to February 2018) period using this PRCCF product. We evaluate the new MISR PRCCF cloud climatology against two other cloud data sets: the original MISR RCCM and Terra MODIS MOD35 (Ackerman & Frey, 2015) confined to within the MISR swath. Both MODIS and MISR are on the Terra satellite (10:30 a.m. Equator Crossing Time [ECT] for the descending node). The MISR swath (360 km) lies within Terra MODIS swath (2,330 km). While our comparison of these three data sets is near global, we select six regions across the globe where the PRCCF diverges substantially from the climatology of the other two data sets for further analysis. In these six regions, 180 ASTER (also on Terra collecting imagery at 15-m × 15-m resolution within the MISR swath) scenes of $60 \times 60\ km^2$ are randomly selected to derive “true” CF for direct evaluation of the MISR PRCCF, RCCM, and MOD35.

2. Data and Methods

In this work, we evaluate resolution-corrected MISR PRCCF against MISR original standard estimate CF (standard estimate cloud fraction [SECF]), MODIS, and ASTER CF. We restrict our analysis within 50°N to 50°S because the MISR RCCM (which feeds into the PRCCF) is not intended for surfaces covered with snow and ice. Over snow and ice, MISR relies on its stereoscopic and angular signature cloud masks for deriving CF (Diner et al., 1999).

2.1. MISR Data and Analysis

MISR views the Earth simultaneously with nine push-broom cameras with widely spaced viewing zenith angles (nominally 0°, ±26.1°, ±45.6°, ±60.0°, and ±70.5°) and using four spectral bands (446, 558, 672, and 866 nm) in each of the nine cameras. A detailed description of the MISR instrument is provided in Diner et al. (1998). We have analyzed Level 2 (L2) CF parameters, namely, PRCCF and SECF obtained from MISR TC-Classifiers cloud products version F07_0012 and F07_0013. Due to an error in the snow-ice mask, the product has been regenerated for the period June 2014 to May 2017 and named as version F07_0013. For all other months, F07_0012 is the current version. Thus, these two versions together provide a consistent record with identical snow and ice mask.

Both PRCCF and SECF are derived at 17.6-km × 17.6-km resolution using RCCM cloud mask (version F04_0025) of pixel size 1.1 km × 1.1 km as input. Each 1.1-km pixel of RCCM cloud mask (Diner et al., 1999; Zhao & Di Girolamo, 2004) is considered high confidence cloudy, low confidence cloudy, high confidence clear, low confidence clear, or no retrieval. High and low confidence cloud is used for computing 17.6-km resolution cloud fractions. The RCCM is generated for each of MISR's nine cameras. Here, only the CFs derived from MISR's nadir camera are used to keep the viewing geometry and sampling time nearly coincident with MODIS and ASTER. The SECF is simply the ratio of cloudy pixels to total number of pixels. The PRCCF field is derived using a machine learning, pattern recognition technique that uses the 1.1-km resolution RCCM as input and trained using high-resolution ASTER over selected regions of the world as fully described in Jones et al. (2012). Further discussion on this training set is given in sections 3 and 4. The PRCCF technique essentially makes use of spatial patterns of cloudiness observed at course resolution to correct for the cloud fraction bias caused by the resolution effect, since this bias is known to be strongly tied to the spatial pattern of cloudiness (Di Girolamo & Davies, 1997).

We have regridded the L2 data at 0.5° × 0.5° resolution using MISR Ancillary Geographical Product (AGP) to generate CF data at a daily scale, from which we calculate the CF climatology for winter (December, January, and February [DJF]), spring (March, April, and May [MAM]), summer (June, July, and August [JJA]), and fall (September, October, and November [SON]) using 18 years (March 2000 to February 2018) of uncorrected and resolution-corrected MISR cloud products. There are already existing L3 MISR total CF data (CFbA—Cloud Fraction by Altitude) at daily, monthly, seasonal, and annual scales with the same spatial resolution of 0.5° × 0.5° (Di Girolamo et al., 2010). However, we did not use that data set as we need space-time coherent L2 swath data for accomplishing pixel-wise collocation process of MISR-MODIS and MISR-ASTER. The collocation process is described in section 2.4.

2.2. MODIS Data and Analysis

MODIS is a passive remote sensing instrument onboard Terra with MISR (Barnes et al., 1998). It has 36 spectral channels with cross-track scanning over a 2,330-km swath compared to MISR's much narrower swath of 360 km. MODIS cloud fractions have been reported to have a large view angle effect, with cloud fractions increasing substantially toward swath edge (Maddux et al., 2010). Therefore, in the present study, MODIS CF has been derived only from MODIS pixels that lie within the MISR swath. For this, MOD35 (collection 6.1) cloud mask of resolution 1-km × 1-km pixel size (Ackerman & Frey, 2015) along with MODIS geolocation product (MODIS Characterization Support Team (MCST), 2017) MOD03 (collection 6.1) has been used. From MOD35, we considered “clear” and “probably clear” category as clear pixels and “cloudy,” and “probably cloudy” as cloudy pixels in computing cloud fraction over the same 0.5° × 0.5° grid used in the MISR analysis, which is consistent with how CF climatologies are derived from MODIS (e.g., Stubenrauch et al., 2012). Only descending node MODIS granules are selected to match with MISR daytime collection, and only MODIS data that fall within the MISR swath (viewing zenith angles <18°) are used. To check the differences in CF between full swath and 18° swath, the full-swath standard MODIS CF (1° × 1°) product from GEWEX database (Stubenrauch et al., 2012) has been used.

2.3. ASTER Data and Analysis

ASTER, a passive sensor flying onboard Terra along with MISR and MODIS, produces about 650 scenes per day with each scene having an area of 60 km × 60 km. Details of the ASTER instrument and its performance are documented in Abrams (2000). There are two cameras in ASTER. One camera pointing near nadir has three visible and near-infrared (VNIR) spectral bands (0.5 to 1.0 mm) with 15-m spatial resolution, six short-wave infrared (SWIR) spectral bands (1.0 to 2.5 mm) with 30-m spatial resolution, and five thermal infrared (TIR) spectral bands (8 to 12 mm) with 90-m spatial resolution. The other camera, pointing backward in the along-track direction, has only one spectral band (0.78 to 0.86 mm) with 15-m spatial resolution.

The ASTER cloud masks used here are generated using a single threshold applied to the 3 N channel (760–860 nm, nadir view) over a 60-km × 60-km scene following the same procedure described in earlier studies (Dey et al., 2008, 2011; Jones et al., 2012; Zhao & Di Girolamo, 2006, 2007). In short, for each scene, the threshold is manually selected by simultaneously visualizing the radiance and cloud mask images to verify the chosen threshold. An example of cloud masking for an ASTER scene is shown in Figure S1 in the supporting information (SI). The threshold is considered as correct (e.g., $DN = 31$ in Figure S1) if negligible change in cloud mask occurred by visual inspection when it is shifted in either direction, and the mask is judged to accurately represent the cloud distribution in the radiance image. At 15-m spatial resolution, we assume that each pixel is either completely cloud covered or completely clear in computing cloud fraction and take this as the benchmark for scene-by-scene comparison with MISR and MODIS. As discussed in the aforementioned studies, there is some unquantified uncertainty associated with this benchmark of scene-level CF. Therefore, in the interest of reproducibility, the scene thresholds for all 180 ASTER scenes used in this study are given in SI (Table S1).

10.1029/2020GL090313

2.4. ASTER, MISR, and MODIS Collocation

To evaluate the MISR and MODIS CF against ASTER CF, co-location is needed. ASTER (15 m) and MOD35 (1 km) pixels are collocated with MISR 17.6-km cloud fraction pixels for getting one-to-one pixel-wise comparison and for robust evaluation of MISR PRCCF. The MISR PRCCF and SECF are provided at 17.6-km resolution within the MISR TC_Classifiers product. To make a proper comparison between MISR PRCCF and the original CF (SECF) with the ASTER CF, ASTER-MISR collocation is done for each scene. There are a minimum four and maximum nine 17.6-km × 17.6-km MISR pixels coincident within an ASTER scene, where the number of 15-m × 15-m ASTER pixels is more than or equal to 99% of the total possible number of ASTER pixels in a 17.6-km × 17.6-km subscene area. We have done this collocation process individually for each 180 ASTER scenes. This resulted in a total 1,211 MISR subscenes (17.6 km × 17.6 km) collocated with 180 (60 × 60 km^2) ASTER scenes fulfilling above-mentioned criteria.

The MOD35 1-km × 1-km pixels are also collected for each 17.6-km × 17.6-km pixels of MISR. Thus, for each 17.6-km MISR pixel (within an ASTER scene), we have one PRCCF, one SECF, one ASTER CF, and one MOD35 CF value.

3. Results

We first discuss a comparative study among MISR and MODIS CFs, followed by their differences and changes in CFs after correcting resolution and view angle effect in section 3.1. In section 3.2, selected regions are looked at more closely to compare MISR and MODIS CF with ASTER-derived CF.

3.1. MISR PRCCF, MISR SECF, and MOD35 (Within MISR Swath) CFs and Their Differences

We first reduce the bias in MODIS CF caused by "view angle effect" before carrying out the comparative assessment. Satellite data sets have discrepancies among themselves due to view angle differences. For example, the MODIS CF increases from 0.57 to 0.71 between nadir and edge-of-scan (~67°) observations for clouds observed between 35°N and 35°S latitude (Maddux et al., 2010). The increase in CF occurs because the more oblique views (1) observe more cloud sides, (2) have a larger instantaneous field of view, and (3) are more sensitive to detecting thin clouds. As MODIS has a very wide swath (2,330 km) compared to MISR (360 km), we have taken only those MODIS pixels that fall within MISR swath. This has resulted in a reduction in MODIS CF for all seasons (Figure S2b) between 50°S and 50°N of 0.07 (from 0.66 to 0.59), with regional changes reaching as high as 0.4. The largest changes occur over regions and seasons known to be dominated by cumulus or thin cirrus.

Considering only the MODIS data within the MISR swath, the spatial patterns of seasonal MISR PRCCF, MOD35 CF, and SECF are compared in top panel of Figure 1, with differences between these plots presented at the bottom panel of Figure 1. In general, the spatial patterns of cloud coverage for all seasons match quite well. But it is clear that over the majority of Earth's surface, PRCCF < MOD35 (within MISR swath) < SECF. Over some of the land regions (like some parts of South America and Africa), MOD35 (within MISR swath) > SECF. Since the RCCM and MOD35 cloud masking are done at comparable resolution (1.1-km and 1-km pixel resolution, respectively), and we have confined the MODIS data to within the MISR swath, the differences between SECF and CF derived from MOD35 (within MISR swath) are mainly induced from "instrument sensitivity" to cloud detection and "methodology" of cloud masking. Over oceanic regions, for all seasons, SECF is greater than MOD35 (within MISR swath), with regional differences typically between 0.05 and 0.3 (column SECF-MOD35 within MISR swath in Figure 1). This verifies that MISR's RCCM clear-conservative cloud detection is more likely to label a pixel containing a subpixel cloud as cloudy compared to MOD35 (Zhao & Di Girolamo, 2006). Over land, positive regional differences are found in regions where cloud cover is dominated by cumulus clouds owing to the clear-conservative nature of the RCCM. There are also positive differences in regions and seasons when the surface is covered with snow since the RCCM cannot distinguish between snow and cloud, whereas MOD35 is more capable. On the other hand, the negative regional differences are dominated by optically thin clouds, where failure in the RCCM to detect thin clouds, relative to MODIS, occurs owing to the limited spectral information of MISR for cloud detection coupled with the high degree of spatial and temporal variability of land surface reflectance (Stubenrauch et al., 2012).

10.1029/2020GL090313

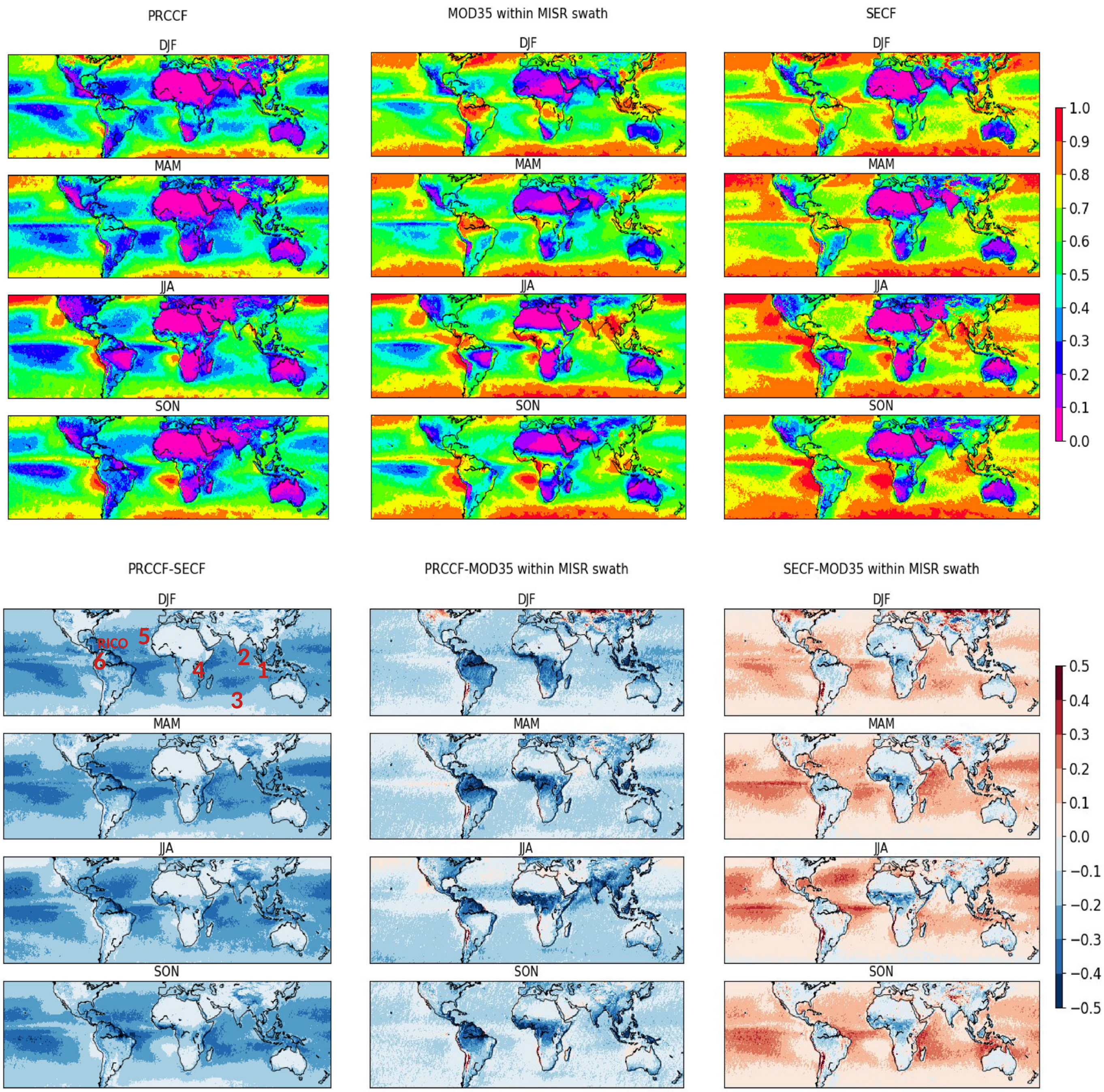

Figure 1. Top panel: Spatial distributions of CF from MISR PRCCF, MOD35 CF within MISR swath, and MISR SECF. Bottom panel: CF differences between MISR PRCCF, MOD35 CF within MISR swath, and MISR SECF. The region spans 50°N and 50°S, 180°W and 180°E. Four seasons (DJF, MAM, JJA, and SON) are shown and are averages from March 2000 to February 2018. Locations of six regions selected for ASTER data analysis and the RICO region used in Jones et al. (2012) are shown in the top plot of column PRCCF-SECF.

The absolute difference between PRCCF and SECF (i.e., the reduction in CF due to resolution correction) is shown in column PRCCF-SECF of Figure 1. It is observed that after the resolution effect correction, CF reductions are largest (0.3–0.5) in regions known to be dominated by cumulus clouds and smallest (<0.1) in cloudy regions known to be dominated by stratiform clouds as well as desert areas. Such a large reduction in CF over the tropical oceans is important in the context of climate sensitivity to fractional cloud cover. The seasonal reduction is prominent over the Indian monsoon region during monsoon (JJA) and over the Amazonia and the rest of South America during December–May.

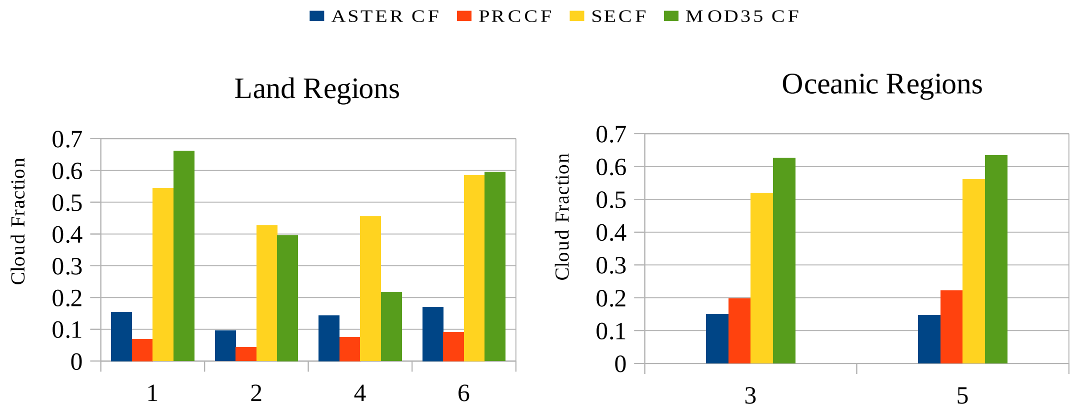

Figure 2. Mean CF from collocated pixels of ASTER, PRCCF, and SECF and MOD35 over the lands and oceanic regions. The numbers in *x* axis denote the regions where ASTER scenes are chosen (shown in the top plot of PRCCF-SECF column in Figure 1).

While the PRCCF-SECF differences are strictly due to the resolution effect, the PRCCF-MOD35 differences are due to cloud detection sensitivity differences between RCCM and MOD35, as well as resolution effects in MOD35 CF. Figure 1 shows the differences between PRCCF and MOD35 CF (within MISR swath) for each season. We see that, after resolution correction, the RCCM-derived CF (PRCCF) is much closer to MOD35 CF over oceanic regions as compared to the RCCM-derived SECF, as would be expected from the study of Zhao and Di Girolamo (2006). The differences with MOD35 CF range between 0 and −0.2 compared to 0 to −0.4 for the SECF. Over land, the differences between MOD35 (within MISR swath) and PRCCF in many snow-free regions are even more negative than SECF-MOD35 differences, particularly in regions dominated by cirrus, presumably because of the lower cloud detection sensitivity over land of the RCCM compared to MOD35 (Stubenrauch et al., 2012).

Table S3 shows the CF statistics from SECF, PRCCF, MODIS-full-swath (shown in Figure S2a in SI), and MODIS-within-MISR-swath. Annual averages between 50°S and 50°N of CF derived from SECF, PRCCF, and MOD35 (within MISR swath) are 0.65, 0.47, and 0.59, respectively. While considering the near-global average, PRCCF, SECF, and MOD35 (within MISR swath) CF do not exhibit much seasonal variability. Rather, there are large differences in annual mean averages among these data sets: a reduction in annual mean CF of 0.07 from MODIS-full-swath to MODIS-within-MISR-swath and a reduction in annual mean CF of 0.18 and 0.12 relative to MISR SECF and MODIS-within-MISR-swath, respectively, after correcting for the resolution effect. Such a large change in CF due to resolution effects warrants a closer look, which is shown in the next section.

3.2. Evaluation Against “True” CF Derived From ASTER

The PRCCF-SECF in the bottom panel of Figure 1 shows regions of significant differences between PRCCF and SECF with some regions showing a spread among the data sets nearing 0.40 in CF for all seasons. Here we use the ASTER data to further examine six selected regions (four over land and two over the ocean). The six regions have been chosen based on the following criteria: (1) a region where ASTER routinely collects data, (2) a spatially uniform surface to better facilitate our ASTER cloud masking method, (3) regions where boundary layer clouds often occur, (4) and large (>0.20) reduction in CF post resolution-effect correction. We did not choose the tropical western Atlantic, the Gulf of Mexico, or the north-western Indian Ocean since those are the regions where the training data were derived from for the PRCCF (Jones et al., 2012). For each of the six regions, 30 randomly selected ASTER scenes were chosen for cloud masking, which were enough samples to ensure that the standard error in the mean CF of the sample population was less than a few percent. For scenes where we were unable to create a reliable ASTER cloud mask, the scene was discarded and another random scene was selected. Scenes that contain intense sun glint or strong gradients of sun glint create difficulties in selecting an accurate threshold for cloud masking. However, some scenes containing sun glint remained in the data set if thresholding could be done to produce a reliable cloud mask. The file name, location, and cloud mask threshold for each ASTER scene are provided in SI (Table S1).

The mean CFs derived from the ASTER cloud masks and the corresponding collocated PRCCF and SECF products along with MOD35 CF over the land and oceans are compared in Figure 2. Table S2 in SI provides the mean (±1 standard deviation) CF for ASTER, PRCCF, SECF, and MOD35 for each selected region. Overall, the PRCCF CF is observed to be within 0.05–0.08 of ASTER CF but with a dual bias. Over the land regions (Indonesia, Sri Lanka, Tanzania, and Colombia denoted as numbers 1, 2, 4, and 6, respectively, at the top plot of column PRCCF-SECF in Figure 1), PRCCF is found to be lower than ASTER CF by 0.05–0.08, whereas SECF and MOD35 CF always overestimate true CF by a large margin (~0.4–0.5). Over the oceanic regions (Indian Ocean and North Atlantic Ocean denoted as numbers 3 and 5, respectively, at the top plot of column PRCCF-SECF in Figure 1), PRCCF is higher than ASTER CF by 0.05–0.07, whereas the overestimation of SECF and MOD35 CF goes up to ~0.5 on average. Therefore, we conclude that there is a significant improvement in the estimation of CF by the PRCCF relative to the MISR SECF and the MOD35 CF as it relates to the resolution effect on CF measurements.

4. Discussion and Conclusions

Cloud feedback, or in particular tropical shallow cloud feedback, is a major source of uncertainties in model estimated climate sensitivity (Bony & Dufresne, 2005; Klein et al., 2017; Vial et al., 2013). Reducing these uncertainties requires highly accurate and stable observations over decades, especially targeting trade cumulus regions (Bony et al., 2017; Winker et al., 2017). Our current suite of global cloud climatologies from satellites reports total mean cloud fraction ranging from 0.56 to 0.73, with regional difference topping 0.4 (Stubenrauch et al., 2012). The effects of sensor resolution, sensor view angle, diurnal cycles, and instrument sensitivity and methodological choices all come into play trying to understand the large spread among estimates of total cloud fraction reported by these satellite data sets. In the present study, we examine the newly built resolution effect-corrected MISR CF (PRCCF) against the original MISR CF (SECF) and the MODIS-Terra CF. We found a large reduction in CF across various regions of the globe due to the resolution correction, with reductions >0.4 in regions dominated by shallow cumulus clouds. Between 50°N and 50°S, the annual mean CF is 0.47 from the new resolution-corrected product, compared to 0.65 from MISR's original product and 0.59 from Terra-MODIS that falls within the MISR swath. Note that we have accounted for the sensor view angle effect by confining the MODIS data to be within the MISR swath. This alone reduced to the annual mean total CF between 50°N and 50°S from 0.66 to 0.59 between MODIS-full-swath and MODIS-within-MISR-swath. Any remaining sensor view angle effects across the 18° swath of MISR are expected to be less than 0.01 for both MODIS (Maddux et al., 2010) and MISR (Zhao & Di Girolamo, 2004). Diurnal effects are not an issue in our comparison between products since MISR and MODIS are both on Terra, and we confined the analysis to within the MISR swath (and recognizing that this is a mid-morning climatology tied to the 10:30 a.m. ECT of the Terra orbit). In comparing the resolution-corrected CF from MISR to the original CF from MISR, the sensitivity to cloud detection is the same—only resolution correction is done within the MISR PRCCF. In comparison to MODIS, however, instrument sensitivity and methodology differences relative to MISR remain. Since resolution effects remain within MODIS CF and is positive, its annual mean CF of 0.59 between 50°S and 50°N is an overestimate compared to the annual mean of 0.47 derived from resolution effect-corrected MISR PRCCF.

We further assessed the accuracy of the CF products against 180 randomly selected scenes of 15-m resolution ASTER data over six selected regions where maximum CF reduction is observed. The MISR resolution-corrected CF lies within ±0.05–0.08 of this benchmark data, where MISR uncorrected CF and MODIS CF overestimated this benchmark by 0.40–0.50. This provides clear evidence on the improvements had by the new MISR PRCCF product over the original MISR and MODIS CF products, at least in terms of resolution correction. Still, the ±0.05–0.08 error in the mean CF in these regions is quite large and larger than the ±0.01 error in the mean CF reported in Jones et al. (2012) based on data collected in the same region and seasons as the training data. We speculate that the larger error found in our study is due to the limited coverage of the Jones et al. (2012) training data (i.e., covering only ocean regions of the tropical Western Atlantic, parts of the Indian Ocean, and the Gulf of Mexico) used by the MISR PRCCF product. It suggests that some of the cloud patterns (e.g., size, shape, and spatial distribution) found in the regions examined in Figure 2, which include both land and ocean regions, are not found within the training data used by the MISR PRCCF. If so, then we recommend developing a more representative training data from ASTER to be used by the MISR PRCCF.

Our results, specifically the large reduction in near-global (within 50 N to 50S) annual CF after resolution effect correction, have several implications for climate science. First, most climate models (e.g., Dolinar et al., 2015) tend to underestimate CF when compared against traditional satellite data sets. Our results suggest a reevaluation of climate model cloud fraction bearing in mind issues that may bias satellite-derived cloud fraction, including sensor resolution. Second, net cloud radiative forcing strongly depends on CF (Dong et al., 2010; Saud et al., 2016). An improved CF climatology and representation of this climatology in climate models would lead to more accurate estimates of cloud forcing. Third, the misrepresentation of cloud feedback (i.e., changes in CF in response to climate forcing that in turn affects cloud characteristics) in climate models is a major source of uncertainty in projecting future climate. Observationally constrained estimates of cloud feedback (e.g., Zhou et al., 2013) that are used to evaluate model performances may improve with a better CF product. Finally, more accurate CF data would lead to a robust interpretation of aerosol-cloud interaction in satellite-based studies (e.g., Gryspeerdt et al., 2016).

Data Availability Statement

Data for producing Figures 1, 2, S1, and S2 are available in the Mendeley data repository (https://doi.org/10.17632/k36f6tsvp5.1).

Acknowledgments
This work is partially supported by the MISR project through the Jet Propulsion Laboratory of the California Institute of Technology under contract 1474871 and the NASA ACCESS program under contract NNX16AMO7A. We acknowledge Langley Research Center (LaRC) for MISR L2 CF products (https://asdc.larc.nasa.gov/data/MISR/MIL2TCCL.003/), MISR AGP data (https://l0dup05.larc.nasa.gov/MISR/cgi-bin/MISR/main.cgi), and LAADS DAAC data archive (https://ladsweb.modaps.eosdis.nasa.gov/archive/allData/61/) for MOD35_L2 and MOD03 data. We also acknowledge LPDAAC for ASTER data (https://lpdaac.usgs.gov/products/ast_l1bv003/) and https://climserv.ipsl.polytechnique.fr/gewexca/DATA/instruments/MODIS-ST/ for standard MODIS L3 CF product. S. D. acknowledges IIT Delhi for financial support for the Institute Chair Professor.

References

Abrams, M. (2000). The advanced spaceborne thermal emission and reflection radiometer (ASTER): Data products for the high spatial resolution imager on NASA's Terra platform. *International Journal of Remote Sensing*, *21*(5), 847–859. https://doi.org/10.1080/014311600210326

Ackerman, S. A., & Frey, R. (2015). MODIS atmosphere L2 cloud mask product. NASA MODIS Adaptive Processing System, Goddard Space Flight Center, USA. https://doi.org/10.5067/MODIS/MOD35_L2.006

Barnes, W. L., Pagano, T. S., & Salomonson, V. V. (1998). Prelaunch characteristics of the moderate resolution imaging spectroradiometer (MODIS) on EOS-AM1. *IEEE Transactions on Geoscience and Remote Sensing*, *36*(4), 1088–1100. https://doi.org/10.1109/36.700993

Bony, S., & Dufresne, J. L. (2005). Marine boundary layer clouds at the heart of tropical cloud feedback uncertainties in climate models. *Geophysical Research Letters*, *32*, L20806. https://doi.org/10.1029/2005GL023851

Bony, S., Stevens, B., Ament, F., Bigorre, S., Chazette, P., Crewell, S., et al. (2017). EUREC4A: A field campaign to elucidate the couplings between clouds, convection and circulation. *Surveys in Geophysics*, *38*(6), 1529–1568. https://doi.org/10.1007/s10712-017-9428-0

Dey, S., Di, G. L., Zhao, G., Jones, A. L., & McFarquhar, G. M. (2011). Satellite-observed relationships between aerosol and trade-wind cumulus cloud properties over the Indian Ocean. *Geophysical Research Letters*, *38*, 01804. https://doi.org/10.1029/2010GL045588

Dey, S., Di Girolamo, L., & Zhao, G. (2008). Scale effect on statistics of the macrophysical properties of trade wind cumuli over the tropical western Atlantic during RICO. *Journal of Geophysical Research*, *113*, D24214. https://doi.org/10.1029/2008JD010295

Di Girolamo, L., & Davies, R. (1997). Cloud fraction errors caused by finite resolution measurements. *Journal of Geophysical Research*, *102*(D2), 1739–1756. https://doi.org/10.1029/96JD02663

Di Girolamo, L., Menzies, A., Zhao, G., Mueller, K., Moroney, C., & Diner, D. J. (2010). Multi-angle Imaging SpectroRadiometer Level 3 Cloud Fraction by Altitude Algorithm Theoretical Basis Document (JPL Publ. D-62358, pp. 1–24). Pasadena, CA: Jet Propulsion Laboratory.

Diner, D. J., Beckert, J. C., Reilly, T. H., Bruegge, C. J., Conel, J. E., Kahn, R. A., et al. (1998). Multi-angle Imaging SpectroRadiometer (MISR) instrument description and experiment overview. *IEEE Transactions on Geoscience and Remote Sensing*, *36*(4), 1072–1087. https://doi.org/10.1109/36.700992

Diner, D. J., Di Girolamo, L., & Clothiaux, E. (1999). Multi-angle Imaging SpectroRadiometer Level 1 Cloud Detection Algorithm Theoretical Basis, JPL Publ. D-13397, Rev. B (p. 38). Pasadena, CA: Jet Propulsion Laboratory.

Dolinar, E. K., Dong, X., Xi, B., Jia, J. H., & Su, H. (2015). Evaluation of CMIP5 simulated clouds and TOA radiation budgets using NASA satellite observations. *Climate Dynamics*, *44*, 2229–2247. https://doi.org/10.1007/s00382-014-2158-9

Dong, X., Xi, B., Crosby, K., Long, C. N., Stone, R., & Shupe, M. (2010). A 10-yr climatology of Arctic cloud fraction and radiative forcing at Barrow, Alaska. *Journal of Geophysical Research*, *115*, D12124. https://doi.org/10.1029/2009JD013489

Eastman, R., & Warren, S. G. (2014). Diurnal cycles of cumulus, cumulonimbus, stratus, stratocumulus, and fog from surface observations over land and ocean. *Journal of Climate*, *27*, 2386–2404. https://doi.org/10.1175/JCLI-D-13-00352.1

Goodman, A. H., & Henderson-Sellers, A. (1988). Cloud detection and analysis: A review of recent progress. *Atmospheric Research*, *21*, 203–228. https://doi.org/10.1016/0169-8095(88)90027-0

Gryspeerdt, E., Quaas, J., & Bellouin, N. (2016). Constraining the aerosol influence on cloud fraction. *Journal of Geophysical Research: Atmospheres*, *121*, 3566–3583. https://doi.org/10.1002/2015JD023744

IPCC (2013). In T. F. Stocker, et al. (Eds.), *Climate change 2013: The physical science basis*. *Contribution of working group I to the fifth assessment report of the intergovernmental panel on climate change* (p. 1535). Cambridge, United Kingdom and New York, NY, USA: Cambridge University Press. https://doi.org/10.1017/CBO9781107415324

Jones, A. L., Di Girolamo, L., & Zhao, G. (2012). Reducing the resolution bias in cloud fraction from satellite derived clear-conservative cloud masks. *Journal of Geophysical Research*, *117*, D12201. https://doi.org/10.1029/2011JD017195

Klein, S. A., Hall, A., Norris, J. R., & Pincus, R. (2017). Low-cloud feedbacks from cloud-controlling factors: A review. *Surveys in Geophysics*, *38*, 1307–1329. https://doi.org/10.1007/s10712-017-9433-3

Maddux, B. C., Ackerman, S. A., & Platnick, S. (2010). Viewing geometry dependencies in MODIS cloud products. *Journal of Atmospheric and Oceanic Technology*, *27*(9), 1519–1528. https://doi.org/10.1175/2010JTECHA1432.1

Minnis, P. (1989). Viewing zenith-angle dependence of cloudiness determined from coincident GOES east and GOES west data. *Journal of Geophysical Research*, *94*(D2), 2303–2320. https://doi.org/10.1029/JD094iD02p02303

MODIS characterization support team (MCST) (2017). MODIS geolocation fields product. NASA MODIS Adaptive Processing System, Goddard Space Flight Center, USA. https://doi.org/10.5067/MODIS/MOD03.061

Rossow, W. B., Mosher, F., Kinsella, E., Arking, A., Desbois, M., Harrison, E., et al. (1985). ISCCP cloud algorithm intercomparison. *Journal of Applied A Meteorology and Climatology*, *24*(9), 877–903. https://doi.org/10.1175/1520-0450(1985)024<0887:ICAI>2.0.CO;2

Saud, T., Dey, S., Das, S., & Dutta, S. (2016). A satellite-based 13-year climatology of net cloud radiative forcing over the Indian monsoon region. *Atmospheric Research*, *182*, 76–86. https://doi.org/10.1016/j.atmosres.2016.07.017

Stubenrauch, C. J., Rossow, W. B., & Kinne, S. (2012). Assessment of global cloud datasets from satellites: A project of the World Climate Research Programme Global Energy and Water Cycle Experiment (GEWEX) Radiation Panel. WCRP Rep. 23/2012, (p. 176) [Available online at www.wcrp-climate.org/documents/GEWEXCloud_Assessment_2012.pdf.]

Stubenrauch, C. J., Rossow, W. B., Kinne, S., Ackerman, S., Cesana, G., Chepfer, H., et al. (2013). Assessment of global cloud datasets from satellites: Project and database initiated by the GEWEX radiation panel. *Bulletin of the American Meteorological Society*, *94*(7), 1031–1049. https://doi.org/10.1175/BAMS-D-12-00117.1

Vial, J., Dufresne, J. L., & Bony, S. (2013). On the interpretation of inter-model spread in CMIP5 climate sensitivity estimates. *Climate Dynamics*, *41*(11–12), 3339–3362. https://doi.org/10.1007/s00382-013-1725-9

Winker, D., Chepfer, H., Noel, V., & Cai, X. (2017). Observational constraints on cloud feedbacks: The role of active satellite sensors. *Surveys in Geophysics*, *38*(6), 1483–1508. https://doi.org/10.1007/s10712-017-9452-0

Zhao, G., & Di Girolamo, L. (2004). A cloud fraction versus view angle technique for automatic in-scene evaluation of the MISR cloud mask. *Journal of Applied Meteorology and Climatology*, *43*, 860–869. https://doi.org/10.1175/1520-0450(2004)043<0860:ACFVVA>2.0.CO;2

Zhao, G., & Di Girolamo, L. (2006). Cloud fraction errors for trade wind cumuli from EOS-Terra instruments. *Geophysical Research Letters*, *33*, L20802. https://doi.org/10.1029/2006GL027088

Zhao, G., & Di Girolamo, L. (2007). Statistics on the macrophysical properties of trade wind cumuli over the tropical western Atlantic. *Journal of Geophysical Research*, *112*, D10204. https://doi.org/10.1029/2006JD007371

Zhao, G., Di Girolamo, L., Dey, S., Jones, A. L., & Bull, M. (2009). Examination of direct cumulus contamination on MISR-retrieved aerosol optical depth and angstrom coefficient over ocean. *Geophysical Research Letters*, *36*, L13811. https://doi.org/10.1029/2009GL038549

Zhou, C., Zelinka, M. D., Dessler, A. E., & Yang, P. (2013). An analysis of the short-term cloud feedback using MODIS data. *Journal of Climate*, *26*(13), 4803–4815. https://doi.org/10.1175/JCLI-D-12-00547.1